Anton Paar

MEASURING INSTRUMENTS FOR YOUR HARD COATINGS

- Find the solution you need in our industrial portfolio, the broadest on the market
- Set up and operate our robust instruments wherever you need them, in the lab or directly at your production site
- Use reference sample kits to verify instrument performance on your own schedule, giving you results you can rely on
- Get started quicker with an application-specific support database that helps you navigate challenges

Get in touch: **www.anton-paar.com**

ADVANCED MATERIALS INTERFACES
www.advmatinterfaces.de

All-Solid-State Li–S Batteries Enhanced by Interface Stabilization and Reaction Kinetics Promotion through 2D Transition Metal Sulfides

*Xiao Sun, Daxian Cao, Ying Wang, Tongtai Ji, Wentao Liang, and Hongli Zhu**

All-solid-state lithium-sulfur batteries (ASSLSBs) based on sulfide solid-state electrolytes (SSEs) provide prospectively high energy density and safety. However, the low conductivity and sluggish reaction kinetic of sulfur cathode limit its commercialization. The use of carbon additives can improve the electrical conductivity but accelerates the decomposition of SSEs. Herein, a highly conductive carbon fiber decorated with hybrid 1T/2H MoS_2 nanosheets is designed. The high chemical and electrochemical compatibility among MoS_2 and sulfide SSE can greatly improve the stability of the cathode and therefore maintain pristine interfaces. The uniform distribution of electrical-conductive metallic 1T MoS_2 on carbon fiber benefits the electron transfer between carbon and sulfur. Meanwhile, the layered structure of MoS_2 can be intercalated by a large amount of Li ions facilitating ionic and electronic conductivity. In consequence, the charge transfer and reaction kinetics are greatly enhanced, and the decomposition of SSEs is successfully relieved. As a result, the ASSLSB delivers an ultrahigh initial discharge and charge capacity of 1456 and 1470 mAh g^{-1} at 0.05 C individually with ultrahigh coulombic efficiency and maintains high capacity retention of 78% after 220 cycles. The batteries also obtain a remarkable rate performance of 1069 mAh g^{-1} at 1 C.

1. Introduction

Lithium-ion batteries (LiBs) play an important role in daily life, including portable electronics, electric vehicles, and large-scale grid storage.[1] The U.S. government sets a goal that 50% of new U.S. vehicles should be electrically powered by 2030.[2] However, commercial LiBs fabricated based on $LiCoO_2$ cathode, graphite anode, and organic liquid electrolyte show limited energy densities of 250 Wh kg^{-1} and high safety risks.[3] It is urgent to develop safe and high-energy-density batteries, and all-solid-state lithium-sulfur batteries (ASSLSBs) are a highly promising candidate. Lithium–sulfur (Li–S) battery owns an ultrahigh theoretical energy density of 2500 Wh kg^{-1}.[4] However, Li–S batteries are generally facing the low coulombic efficiency and fast capacity decay caused by the severe polysulfide shuttle effects in liquid electrolyte. ASSLSBs thus come to priority due to their merits of 1) eliminating polysulfide shuttle effects; 2) potentially higher energy density than traditional LiBs using liquid electrolytes; and 3) superior safety.

Among various solid-state electrolytes (SSEs), sulfide-based electrolytes are the top candidate for ASSLSBs due to their superior room-temperature ionic conductivities (>1 mS cm^{-1}) and high processibility. Furthermore, sulfide SSEs exhibit good chemical and electrochemical stability with the sulfur; thus, no need to fabricate extra costly and complicated interface engineering on the cathode surface. Unfortunately, although great efforts have been made, the performance of the ASSLSBs are still not comparable with Li–S batteries using liquid electrolyte.[5] The challenges are: 1) low utilization of sulfur caused by low ion and electron conductions in the cathode because sulfur is both electronic and ionic insulating; 2) huge interfacial resistance due to the contact loss caused by the large volume change of sulfur during cycling; 3) sluggish reaction kinetics and higher thermodynamic barriers because of the one-step reaction from S_8 to Li_2S in all-solid-state reactions; and 4) sulfide SSEs behave narrow electrochemical stability window (ESW) of 1.7–2.3 V (vs Li/Li^+), the addition of carbon can accelerate the decomposition of sulfide SSE_S when the voltage exceeds the ESW, resulting in enlarged interface impedance, low capacity, low coulombic efficiency, and poor cycling stability. Porous carbon additives with high surface area have been used to address the first two challenges through enhanced electron conduction, increased reaction sites, and accommodated volume expansion.[6,7] However, the third and fourth challenge is still a lack of attention and investigation in ASSLSBs. It is important to use advanced additives to boost the reaction kinetics of sulfur and relieve the decomposition of SSEs.

Transition metal sulfides have been reported that can significantly boost the reaction kinetics of the Li–S batteries in

X. Sun, D. Cao, Y. Wang, T. Ji, H. Zhu
Department of Mechanical and Industrial Engineering
Northeastern University
360 Huntington Avenue, Boston, MA 02115, USA
E-mail: h.zhu@neu.edu
W. Liang
Kostas Advanced Nanocharacterization Facility (KANCF)
Northeastern University
Burlington, MA 01803, USA

The ORCID identification number(s) for the author(s) of this article can be found under https://doi.org/10.1002/admi.202200539.

DOI: 10.1002/admi.202200539

liquid electrolytes, and MoS_2 is one of the most investigated candidates.[8,9] MoS_2 manifests in three different polymorphs which are defined as trigonal 1T, hexagonal 2H, and rhombohedral 3R. The unique chemical peculiarities of MoS_2 enable its prospective application in ASSLSBs. First, owing to the high ion conductivity obtained after lithiation, MoS_2 has been used as the interface stabilizing layer between the liquid electrolyte and Li metal anode.[10–12] Second, 1T MoS_2 owns 10^5–10^6 times higher electrical conductivity than 2H MoS_2, which benefits the charge transfer.[13] Third, MoS_2 can boost the conversion reaction kinetics of sulfur through a catalyst effect in Li–S batteries.[8,14] Fourth, MoS_2 as a metal sulfide has excellent chemical and electrochemical stability with both sulfur and sulfide SSEs. However, compared to the application in Li–S batteries using liquid electrolytes,[11,15] MoS_2 has rarely been investigated as advanced additives in ASSLSBs.

In this work, we rationally designed a functionalized conductive additive with high surface area, high conductivity, and core–shell carbon fibers decorated with hybrid 1T/2H MoS_2 nanosheets and successfully applied it in ASSLSBs. The high surface area polyacrylonitrile (PAN)-derived porous carbon fibers (PPCF) has been investigated in our previous work.[16] Hybrid 1T/2H MoS_2 nanosheets were vertically grown on PPCF to fabricate MoS_2@PPCF through a hydrothermal method with water as the solvent. The MoS_2@PPCF was then used as the conductive additives in the sulfur cathode in ASSLSBs. The sulfide SSE, $Li_{5.4}PS_{4.4}Cl_{1.6}$, was used due to its ultrahigh ionic conductivity of 7.8 mS cm^{-1}. We systematically investigated its stabilization effect on sulfide SSE and the catalyst effect on the conversion reaction kinetics of sulfur. As a result, the ASSLSBs employed MoS_2@PPCF delivered high performance.

2. Results and Discussion

Figure 1 illustrates the overview of this work. As displayed in Figure 1a, the performance of bare PPCF was investigated in an ASSLSB using the mixture of sulfur, PPCF, and SSE (S-PPCF-SSE) as the cathode. Indium-lithium alloy was utilized as anode due to its excellent stability with sulfide SSE, $Li_{5.4}PS_{4.4}Cl_{1.6}$. Generally, sulfide SSE experiences a degradation if the working potential beyond its ESW. In the cathode, the sufficient contact of SSE with highly electronic conductive PPCF accelerates the SSE degradation, as illustrated in Figure 1b. The degradation products own limited ionic conductivity resulting in gradually increased impedance and dramatically reduced capacity at high current rate. Meanwhile, as shown in Figure 1c, the sulfur experiences an one-step conversion to Li_2S in ASSLSBs. The sluggish reaction kinetic negatively affects the rate performance and electrochemical reaction efficiency.

To solve the abovementioned challenges, we synthesized the MoS_2@PPCF, in which a hybrid 1T/2H MoS_2 nanosheets vertically grown on PPCF, and mixed it with sulfur and SSE (S-MoS_2@PPCF-SSE) to work as cathode in the ASSLSB, as shown in Figure 1d. MoS_2, as a metal sulfide, has excellent chemical and electrochemical stability with both sulfur and sulfide SSEs. The MoS_2 nanosheets cover on the surface of PPCF effectively reduce the direct contact area between SSE and PPCF, which can reduce the degradation of sulfide

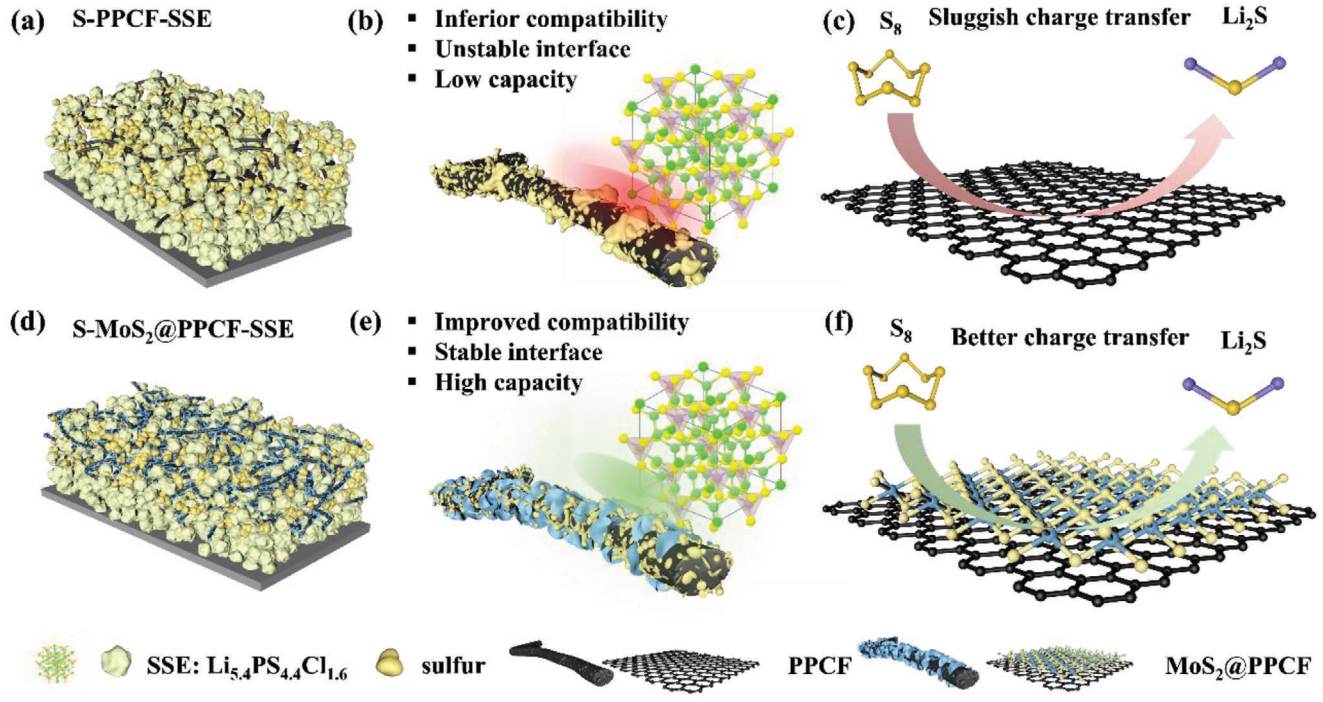

Figure 1. Schematic illustration of the advantages of MoS_2 nanosheets cover on PPCF in the cathode. The configuration of the ASSLSBs using a) S-PPCF-SSE cathode and d) S-MoS_2@PPCF-SSE cathode. The comparison of compatibility and stability with SSE in the cathodes using b) PPCF and e) MoS_2@PPCF as carbon additives in ASSLSBs, individually. The charge transfer comparison in the cathodes using c) PPCF and f) MoS_2@PPCF as carbon additives in ASSLSBs, individually.

SSE (Figure 1e). The stabilized carbon interface benefits the building of high ionic and considerable electronic conduction in the cathode and therefore improves the electrochemical performance. Moreover, MoS_2 is known as a good Li ion conductor whose 2D structure facilitates faster Li-ion diffusion.[17] At the same time, due to the presence of conductive 1T phase MoS_2 and its uniform distribution on PPCF, the considerable electronic conductivity facilitates electron transfer. Meanwhile, the 2H phase MoS_2 can be transformed into the 1T phase after lithiation.[18] With the intercalation of Li ions into the layer distance, both the ionic and electric conductivity of MoS_2 further increase. Therefore, as illustrated in Figure 1f, the MoS_2 on the PPCF is proposed to boost the conversion reaction kinetics of S_8 to Li_2S due to enhanced charge transfer. All these merits enable MoS_2@PPCF a highly promising conductive additive in the sulfur cathode to deliver better performance in ASSLSBs.

Figure 2a shows the synthesis process of MoS_2@PPCF. The PPCF was fabricated with electrospinning followed by stabilization, carbonization, and activation processes, which was reported in our previous work.[16] This PPCF possesses an ultrahigh Brunauer–Emmett–Teller (BET) specific surface area of 1519 $m^2\ g^{-1}$. In addition, PPCF owns a unique core–shell structure where a layer of micropores is located at the fiber surface, which renders remarkable ion accessibility to sulfur,

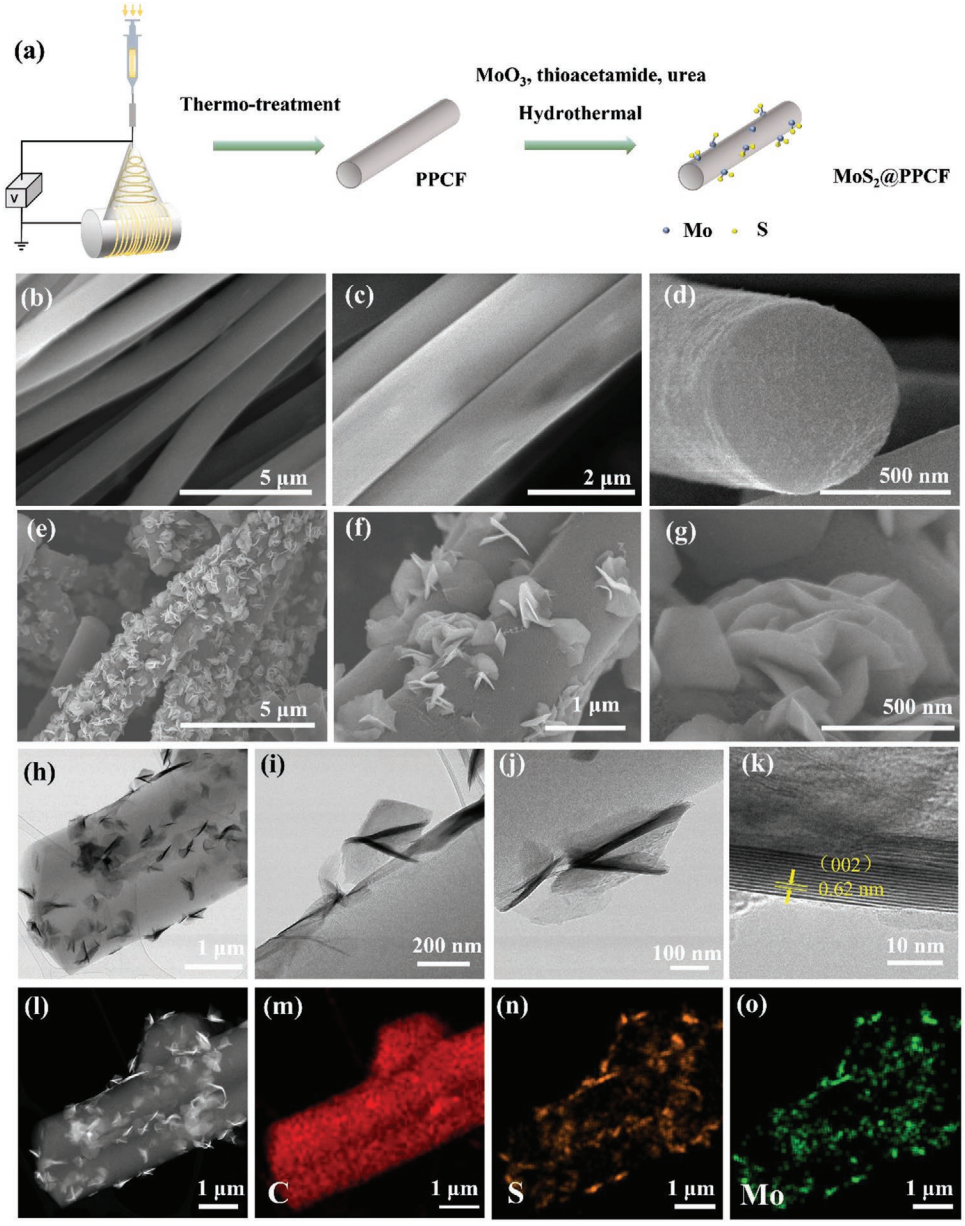

Figure 2. The morphology comparison between PPCF and MoS_2@PPCF. a) The preparation of MoS_2@PPCF through electrospinning, thermo-treatment, and hydrothermal processes. b–d) SEM images of PPCF under different magnifications. e–g) SEM image of vertical MoS_2@PPCF under different magnification. h–j) TEM images of vertical MoS_2@PPCF under different magnification. k) High-resolution TEM image of MoS_2@PPCF. l) TEM image of MoS_2@PPCF and corresponding EDX mapping of m) C, n) S, and o) Mo elements.

contributing to high sulfur utilization. Figure 2b–d displays the scanning electron microscopy (SEM) images of the PPCF at various magnifications. PPCF shows a 1D fibrous morphology, and the average diameter is around 1 µm. When further magnified in Figure 2d, the PPCF shows cross-section morphology that a thin, porous layer covered on the dense fiber core. In comparison, Figure 2e–g displays the SEM images of MoS_2@PPCF with various magnifications. Flower-shaped MoS_2 nanosheets vertically grown and uniformly distributed on the surface of PPCF without aggregation. The MoS_2 owns nanosheets morphology with an average lateral size of ≈300 nm. In Figure 2g, the MoS_2 nanosheets are anchored on the PPCF surface evenly with intimate contact benefiting the fast charge transfer. In contrast, MoS_2 without substrate easily aggregates and leads to poor contact between SSEs and sulfur.[19]

To further validate that the MoS_2 nanosheets are well distributed on PPCF without agglomeration, transmission electron microscopy (TEM) was performed. In Figure 2h, the MoS_2 nanosheets are evenly located on the PPCF, which is consistent with the SEM results. Figure 2i,j displays the multilayer structure of MoS_2. MoS_2, as a typical layered transition metal sulfide, owns sandwiched structure which benefits the fast Li-ion diffusion.[20] Figure 2k shows the high-magnification TEM image of the multilayered MoS_2. The lamellar structure is well defined and the interlayer distance is 0.62 nm which corresponds to the (002) lattice plane of MoS_2.[21] The large interlayer distance of MoS_2, twice as much as the distance in graphite (0.34 nm in graphite[12]), which can promote the Li-ion movement and therefore facilitate a fast Li-ion diffusion. Figure 2i–o displays the TEM image of MoS_2@PPCF and corresponding energy dispersive X-ray (EDX) element mappings of C, S, and Mo. The EDX spectrum of MoS_2@PPCF and atomic fraction table of corresponding elements are shown in Figure S1 (Supporting Information). The ratio of S/Mo is around 2:1, which confirmed the successful synthesis of MoS_2 nanosheets on the carbon fiber.

Figure 3a–c compares the crystal structures of 2H phase and 1T phase MoS_2. 2H MoS_2 and 1T MoS_2 own the hexagonal and trigonal symmetry of the crystal structure, respectively.[22] For 1T phase, the Mo atom is octahedrally coordinated to six neighboring sulfur atoms.[23] In contrast, the Mo atom in 2H phase is prismatically coordinated by six S atoms.[23] Due to different Mo and S atom coordination of octahedral structure with dense active sites, the 1T MoS_2 has 10^5 higher electrical conductivity than the 2H MoS_2.[24] High-resolution TEM was used to analyze the phases of MoS_2 in MoS_2@PPCF. As shown in Figure 3d, the MoS_2 shows a hybrid structure of metallic 1T-MoS_2 phase with trigonal lattice geometry and 2H MoS_2 with common honeycomb lattice geometry. The 1T MoS_2 phase is not as stable as 2H MoS_2 explaining the hybrid phases in MoS_2@PPCF. In addition, a major part of basal planes still exhibits the periodic high-quality crystalline structure of 1T (Figure 3e) and 2H (Figure 3f) hybrid phases, while the partial or complete structural disorder appears at the grain boundaries due to their high surface energy.

Raman spectroscopy was used to study the chemical structure of MoS_2@PPCF, as shown in Figure 3g. Two characteristics peaks located at 378 and 404 cm^{-1} represent E^1_{2g} (due to opposite vibration of two S atoms which respect to the Mo atom) and A_{1g} (due to the vibration of only S atoms in opposite directions) models of 2H MoS_2, respectively.[25] The signal of the 1T MoS_2 may be covered by the strong peak intensity of 2H MoS_2. Note that the ratio of 1T to 2H MoS_2 is difficult to control because the 1T phase is less stable than 2H phase and many conditions affect the content of 1T MoS_2 including the solvent, temperature, pressure, nucleation sites, and purity of the system. Moreover, there are two prominent peaks at 1378 and 1591 cm^{-1} corresponding to the D and G bands of PPCF, respectively. The D and G bands are related to the disordered sp^3 carbon structures and the sp^2 carbon stretching mode. The intensity ratio, I_D/I_G, of MoS_2@PPCF was 0.78 demonstrating the formation of a high proportion of graphitic carbon. Figure 3h displays the X-ray diffraction (XRD) pattern of the MoS_2@PPCF. Compared with the pure PPCF, the MoS_2@PPCF owns obvious peaks at 14.4°, 32.2°, and 58.5° ascribed to the (002), (100), and (110) diffraction peaks of MoS_2, respectively.[26] The sharp peaks further evidence the existence of highly crystalline MoS_2.

Figure 3i displays the thermogravimetric analysis (TGA) profiles of MoS_2@PPCF and PPCF to determine the amount of MoS_2 in MoS_2@PPCF. TGA was conducted from room temperature to 800 °C at the rate of 10 °C min^{-1} in the air atmosphere. The PPCF was totally burnt out, demonstrating high purity. In contrast, there are 15.58 wt% remained in MoS_2@PPCF. The huge weight loss for MoS_2@PPCF, which was due to the oxidation of MoS_2 to MoO_3, occurred at ≈300 °C and the loss of PPCF. According to the calculation, the amount of MoS_2 content in the MoS_2@PPCF composite is 17.33 wt% [Equation (S1), Supporting Information].

The sulfur was then mixed with the SSE and carbon additives, including MoS_2@PPCF and PPCF, to make the S-MoS_2@PPCF-SSE and S-PPCF-SSE cathodes through a ball milling and followed melting infiltration process. The SSE was $Li_{5.6}PS_{4.4}Cl_{1.6}$ which shows a high room temperature ionic conductivity of 7.8 mS cm^{-1} (Figure S2, Supporting Information). Figure S3 (Supporting Information) displays TGA profiles of S-MoS_2@PPCF-SSE, MoS_2@PPCF, sulfur, and SSE to measure the exact ratio of sulfur in the cathode. TGA shows that the element of sulfur content of S-MoS_2@PPCF-SSE composites is 35.7%. **Figure 4**a compares the galvanostatic charge/discharge profiles of ASSLSBs using the S-MoS_2@PPCF-SSE and S-PPCF-SSE as cathodes in the first three cycles at the current rate of C/20. All batteries were cycled at room temperature in the potential range of 0.4–2.4 V (vs In–Li), which corresponds to the voltage range of 1.0–3.0 V (vs Li/Li^+). Obviously, S-MoS_2@PPCF-SSE delivers higher specific capacities and lower polarization than S-PPCF-SSE. The S-MoS_2@PPCF-SSE cathode delivered an ultrahigh discharge (lithiation) capacity of 1456 mAh g^{-1} initially and a high charge (delithiation) capacity of 1470 mAh g^{-1} with an ultrahigh initial coulombic efficiency. The extremely high initial coulombic efficiency is attributed to the stable materials and eliminated shuttle effects. Then the discharge capacity increased to 1531 mAh g^{-1} in the following two cycles, which is due to the better utilization of sulfur. High coulombic efficiencies of ≈99.8% were obtained at second and third cycles, and the charge/discharge profiles were almost overlapping, which suggests the redox reaction owns highly reversibility and superior stability. Moreover, S-MoS_2@PPCF-SSE showed only one pair of charge/discharge plateaus related to the conversion

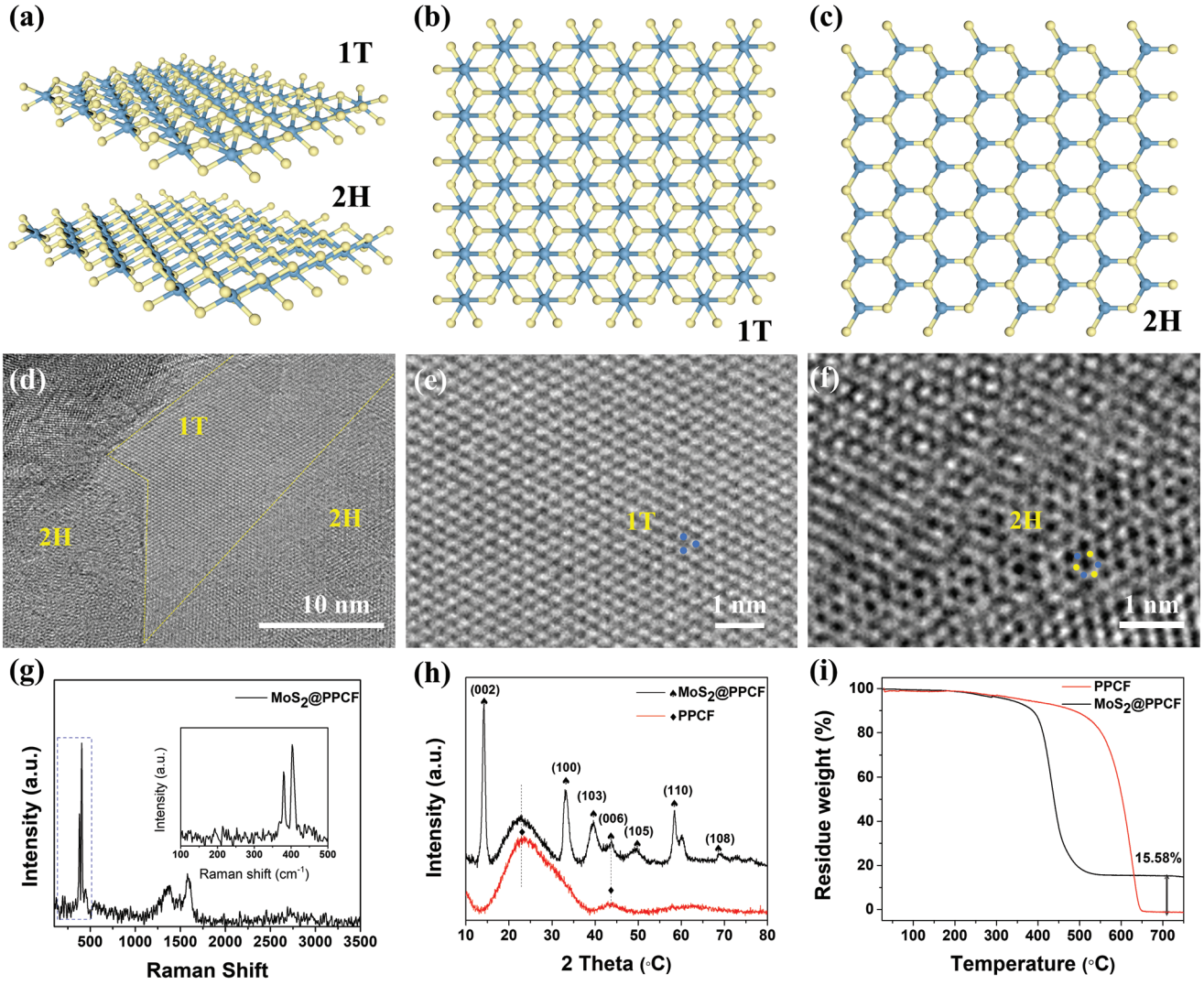

Figure 3. Material characterizations of MoS_2@PPCF. a) The schematic of hybrid 1T/2H MoS_2. The crystal structures of b) metallic 1T-MoS_2 phase with trigonal lattice geometry and c) 2H-MoS_2 phase with common honeycomb lattice geometry. The yellow and blue balls represent S and Mo atoms, respectively. d) TEM images of the hybrid MoS_2 1T and 2H structures. HRTEM images of the MoS_2 in e) 1T and f) 2H phases. The blue and yellow dots illustrate the atom arrangement of Mo and S, respectively. g) Raman spectra of the MoS_2@PPCF. h) XRD patterns of MoS_2@PPCF and PPCF. i) TGA of MoS_2@PPCF and PPCF.

between S_8 and Li_2S, which proved the direct one-step reaction (excluding the formation of lithium polysulfides) in ASSLSBs. In contrast, S-PPCF-SSE only delivered a charge (delithiation) capacity of 1190 mAh g^{-1} and discharge (lithiation) capacity of 1086 mAh g^{-1}, which is much lower than that of S-MoS_2@PPCF-SSE. The initial coulombic efficiency is 109.6%, indicating an extra capacity contribution during charge. The decomposition of sulfide SSE contributes to the extra capacity during charge while accompanied by newborn impedance at the cathodes resulting a sluggish reaction kinetics. Besides the similar plateaus as S-MoS_2@PPCF-SSE, there is an extra plateau observed at 2.8 V (vs Li/Li^+) which coordinates with the SSE decomposition. Considering the narrow ESW of SSE, the SSE experienced a decomposition at high voltage.[27] At the second and third cycles, the extra plateau disappears demonstrating the decomposition of SSE mainly occurs at the first cycle. The differences in these two cathodes demonstrate the MoS_2 layer on PPCF can relieve the decomposition of SSE and boost the utilization of sulfur. At the same time, a cell using MoS_2 as active material was tested to evaluate the capacity contribution of the MoS_2 in the S-MoS_2@PPCF-SSE cell. Figure S4 (Supporting Information) compares the galvanostatic charge/discharge profiles of cells using the MoS_2@PPCF-SSE and S-MoS_2@PPCF-SSE as cathodes at the same current density of 0.27 mA cm^{-2}. The MoS_2@PPCF-SSE delivered a low discharge and charge capacities of 0.18 and 0.03 mAh cm^{-2}. The capacity contribution of MoS_2@PPCF-SSE is only 4.3% during discharge and negligible during charge. This result indicates that the MoS_2 contributes very low to the total electrode capacity.

Figure 4b shows cyclic voltammogram (CV) curves of S-MoS_2@PPCF-SSE in ASSLSBs in the potential range of 1.0–3.0 V (vs Li/Li^+) at various scan rates of 0.10, 0.15, and

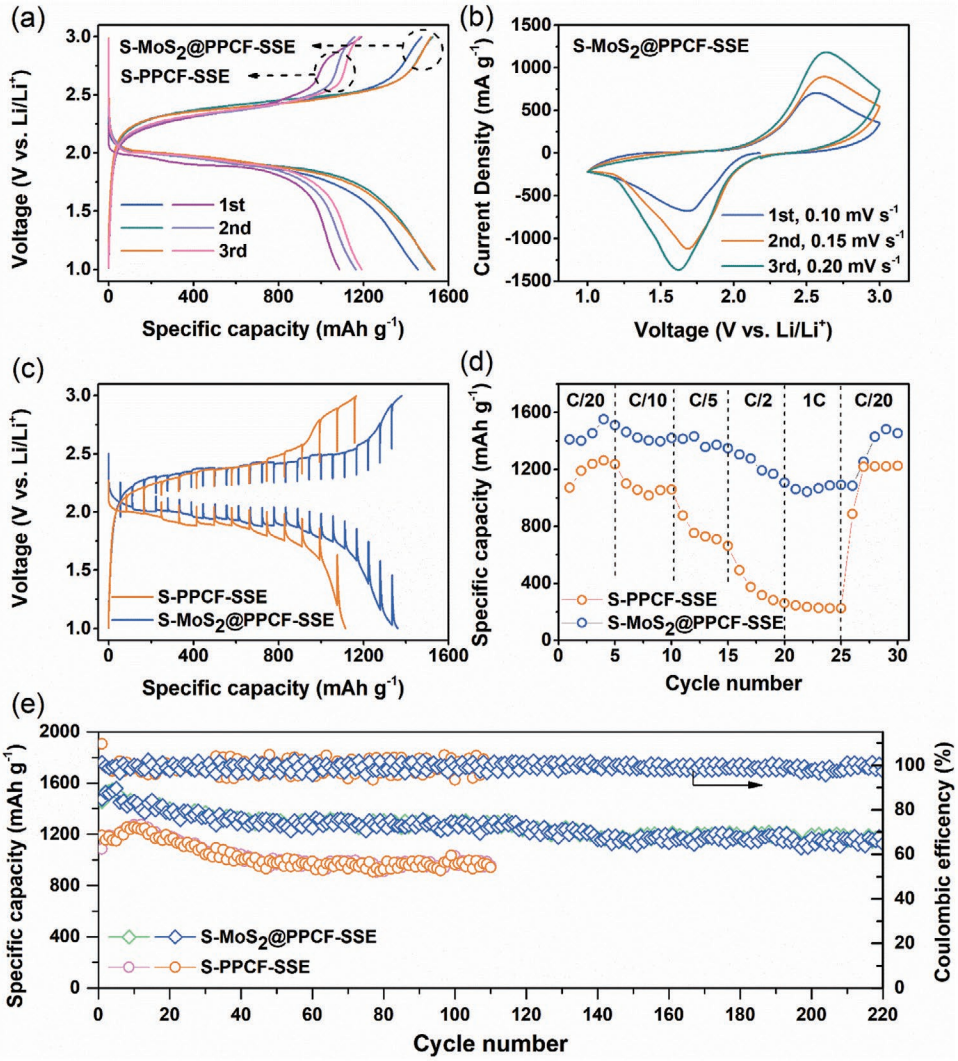

Figure 4. Electrochemical profiles of solid-state Li-In | SE | S-MoS_2@PPCF-SSE and Li-In | SSE | S-PPCF-SSE batteries. a) Galvanostatic charge/discharge profiles of ASLSBs using S-MoS_2@PPCF-SSE and S-PPCF-SSE as cathodes with sulfur loading of 2.9 mg cm^{-2} and the current rate 0.27 mA cm^{-2} (C/20). (b) CV profile of S-MoS_2@PPCF-SSE at a different scan rate of 0.1, 0.15, and 0.2 mV s^{-1} during the first three cycles in ASSLSB. c) GITT profiles of S-MoS_2@PPCF-SSE and S-PPCF-SSE at the rate of C/20. d) Performances at rates ranging from C/20 to 1 C. e) Long-term cycling performance comparison of two solid-state cells at the rate of C/20 for the first three cycles and then adjusted to the rate of C/10 from the fourth cycle. All the cells are tested at room temperature.

0.20 mV s^{-1} individually. In the first cathodic scan at 0.10 mV s^{-1}, one broad reduction peak at 1.7 V (vs Li/Li^+) was detected, contributing to the gradual reduction of sulfur: $S + 2Li^+ + 2e^- \rightarrow Li_2S$. Meanwhile, there was only one oxidation peak at 2.6 V (vs Li/Li^+), corresponding to the oxidation of Li_2S: $Li_2S \rightarrow 2\,Li^+ + S + 2e^-$. In the following cycles, as the scan rates increase, both reduction and oxidation peaks shift a little due to higher polarization. In comparison, Figure S5 (Supporting Information) presents the CV curves of S-PPCF-SSE cell at the same conditions. At 0.1 mV s^{-1}, there were two pairs of obvious oxidation and reduction peaks evidencing the SSE decomposition. As shown in Figure 4C, the galvanostatic intermittent titration technique (GITT) was conducted to evaluate the diffusion and thermodynamic potential of electrochemical reactions.[28] Both S-PPCF-SSE and S-MoS_2@PPCF-SSE cells exhibited a one-step reaction mechanism which coincided well with CV curves. The corresponding polarization values of GITT charge/discharge profile is shown in Figure S6 (Supporting Information). In both the oxidation/reduction processes, when the state of charge (SoC) is smaller than 46.6% (corresponding to specific capacity of 780 mAh g^{-1}), the difference of polarization of these two samples with and without MoS_2 coating is insignificant. However, the polarization difference becomes more obvious when the SoC is larger than 46.6%. The polarization difference between these two cells can further prove the charge transfer and reaction kinetics were greatly enhanced by growing the MoS_2 nanosheets.

Figure 4d compares the rate performances of S-MoS_2@PPCF-SSE and S-PPCF-SSE. The batteries were tested at current rates from 0.05 to 1 C with five cycles at each rate. The S-MoS_2@PPCF-SSE shows significantly higher capacities than the S-PPCF-SSE, especially at high current rates.

The S-MoS_2@PPCF-SSE delivers reversible discharge capacities of 1462, 1401, 1363, 1202, and 1059 mAh g^{-1} at 0.05, 0.1, 0.2, 0.5, and 1 C, respectively. The capacity recovers to 1439 mAh g^{-1} when the cell is recharged at 0.05 C, demonstrating the remarkable rate performance and stability. In comparison, the cell using S-PPCF-SSE cathode exhibits a lower capacity of 1232 mAh g^{-1} at 0.05 C, and the capacity decreased to 220 mAh g^{-1} at 1 C. The boosted rate performance in S-MoS_2@PPCF-SSE was highly attributed to the considerable ion and electron conductivity of MoS_2 during cycling and the excellent compatibility among sulfur, MoS_2, and SSE.

The long cycling performances of S-MoS_2@PPCF-SSE and S-PPCF-SSE at 0.1 C are compared in Figure 4e. Before cycling, all cells were activated at 0.05 C for three cycles. After that, the S-MoS_2@PPCF-SSE achieved high discharge and capacities of 1550 and 1540 mAh g^{-1}, and the capacity maintained stable for 220 cycles with capacity retention of 78%. In contrast, S-PPCF-SE delivers discharge and charge capacities of 1185 and 1153 mAh g^{-1}, respectively. Meanwhile, the capacity of S-PPCF-SSE quickly decreased to 966 mAh g^{-1} in 50 cycles and then keep stable for 110 cycles. The capacity loss may be attributed to the gradually increased impedance caused by the decomposition of SSE. After a stable interface is formed, the capacity is maintained stable.

X-ray photoelectron spectra (XPS) were used to analyze the chemical structure and stability of cathodes in ASSLSBs. **Figure 5**a–c

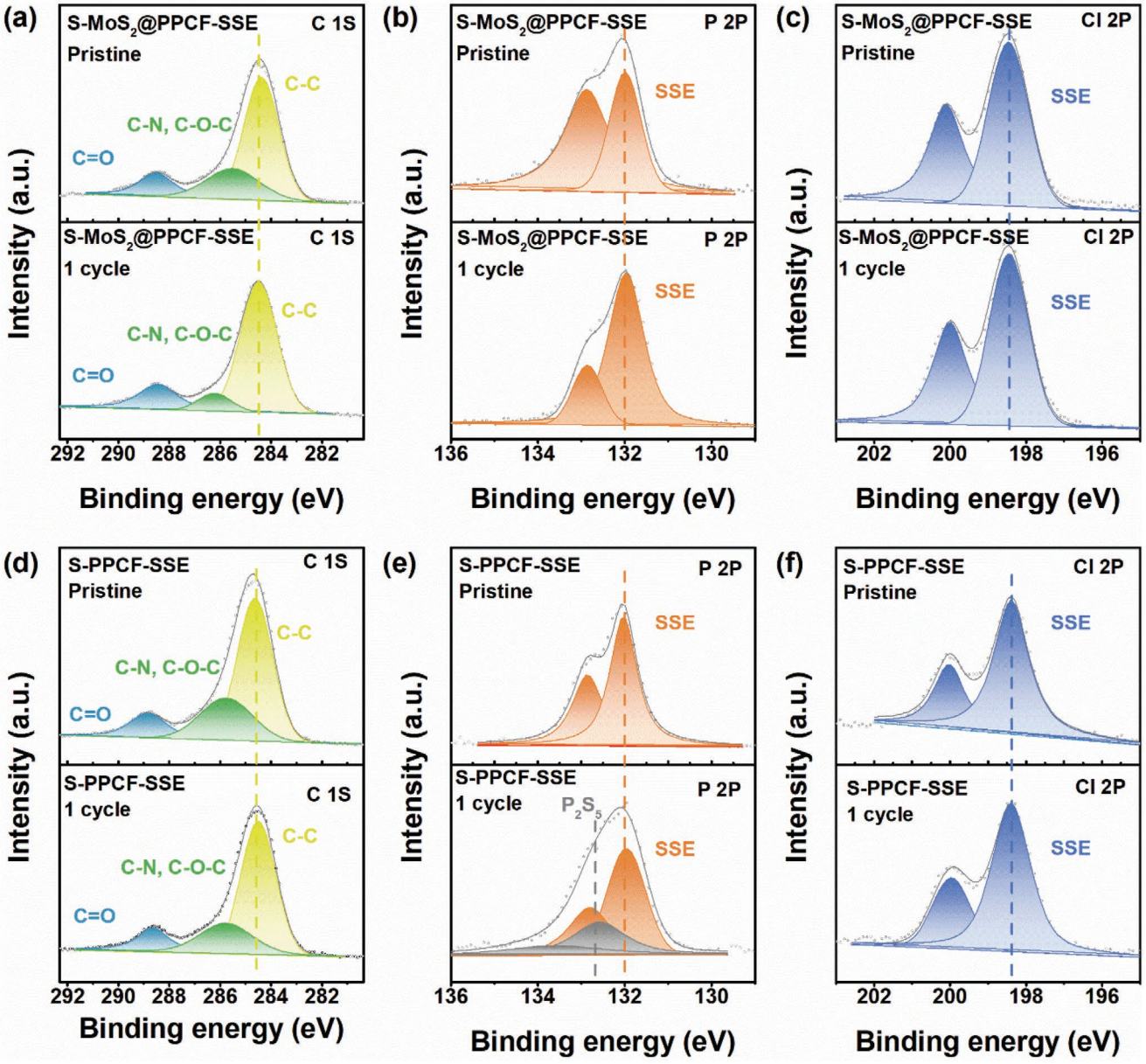

Figure 5. Deconvoluted high-resolution XPS spectra of S-MoS_2@PPCF-SSE and S-PPCF-SSE electrode. a) C 1s XPS spectra of MoS_2@PPCF, b) P 2P XPS spectra of MoS_2@PPCF, c) cl 2P XPS spectra of MoS_2@PPCF, d) C 1s XPS spectra of PPCF, e) p 2p XPS spectra of PPCF, and f) Cl 2p XPS spectra of PPCF.

compares the high-resolution XPS spectra of C, P, and Cl elements in S-MoS_2@PPCF-SSE in pristine and after one cycle in ASSLSB. In Figure 5a, the main component peak is located at 284.5 eV, corresponding to the C=C bond (sp^2). The component peak at 285.9 eV is assigned to the C—N/C—O—C bond peak. The peak at higher bonding energy around 288.8 eV is indexed to the C=O bond peak.[29] No obvious change for the C 1s peak was observed before and after one cycle. evidencing no chemical change. The evolution of high-resolution XPS P 2p spectra is depicted in Figure 5b. The P 2p signals are split into two components due to spin–orbit coupling, which shows a unique $2p_{3/2}$–$2p_{1/2}$ doublet. The P 2p spectrum shows the main doublet with the P $2p_{3/2}$ component located at 132 eV. Investigation of P 2p spectra scan indicates that signature of argyrodite, and it does not show the obvious difference between the pristine cathode and that after one cycle.[30] Figure 5c displays the Cl 2p spectra and main component peak located at 198.4 eV (Cl $2p_{3/2}$), which presents the Cl^- ions. No obvious change occurs for the Cl 2p peak before and after one cycle.[31] Therefore, no chemical change of phosphorus and chlorine chemical is detected, which indicates the stability of SE.

In comparison, XPS was also conducted for S-PPCF-SSE in pristine and after one cycle. The component peaks located at 284.5, 285.9, and 288.9 eV of C 1s spectrum can be indexed to C—C, C—N/C—O—C, and C=O, respectively, which are depicted in Figure 5d.[29] No additional component formed at the pristine state during the investigation of the P 2p spectra scan (Figure 5e). However, upon the full charge of the In-Li|SSE|S-PPCF-SSE cell to 3 V (vs Li/Li^+), an additional component appeared at 132.8 eV in agreement with the P_2S_5 peak from SSE decomposition. These findings agree with the existing literature studies on the oxidation of sulfide SSE.[31,32] Different from the P 2p spectrum, the decomposition product LiCl of argyrodite cannot be detected in the Cl 2p spectrum because its Cl 2p bonding energy is almost the same as SSE.[31]

The morphology evolution of the S-MoS_2@PPCF-SSE before and after cycling was investigated in **Figure 6**. The dispersion of the MoS_2@PPCF, sulfur, and $Li_{5.4}PS_{4.4}Cl_{1.6}$ is very uniform in the pristine state before cycling, as shown in Figure 6a–c. The MoS_2@PPCF was covered by the SE and sulfur, therefore MoS_2 nanosheets cannot be observed clearly, which further proved the intimate contact. Upon the further fully charge of the cell to 3 V (vs Li/Li^+), the electrode looks looser than the fully discharge state due to the delithiation of Li_2S. (Figure 6d–f). However, upon fully discharge of the cell to 1 V (vs Li/Li^+), the volume increases significantly due to the lithiation and

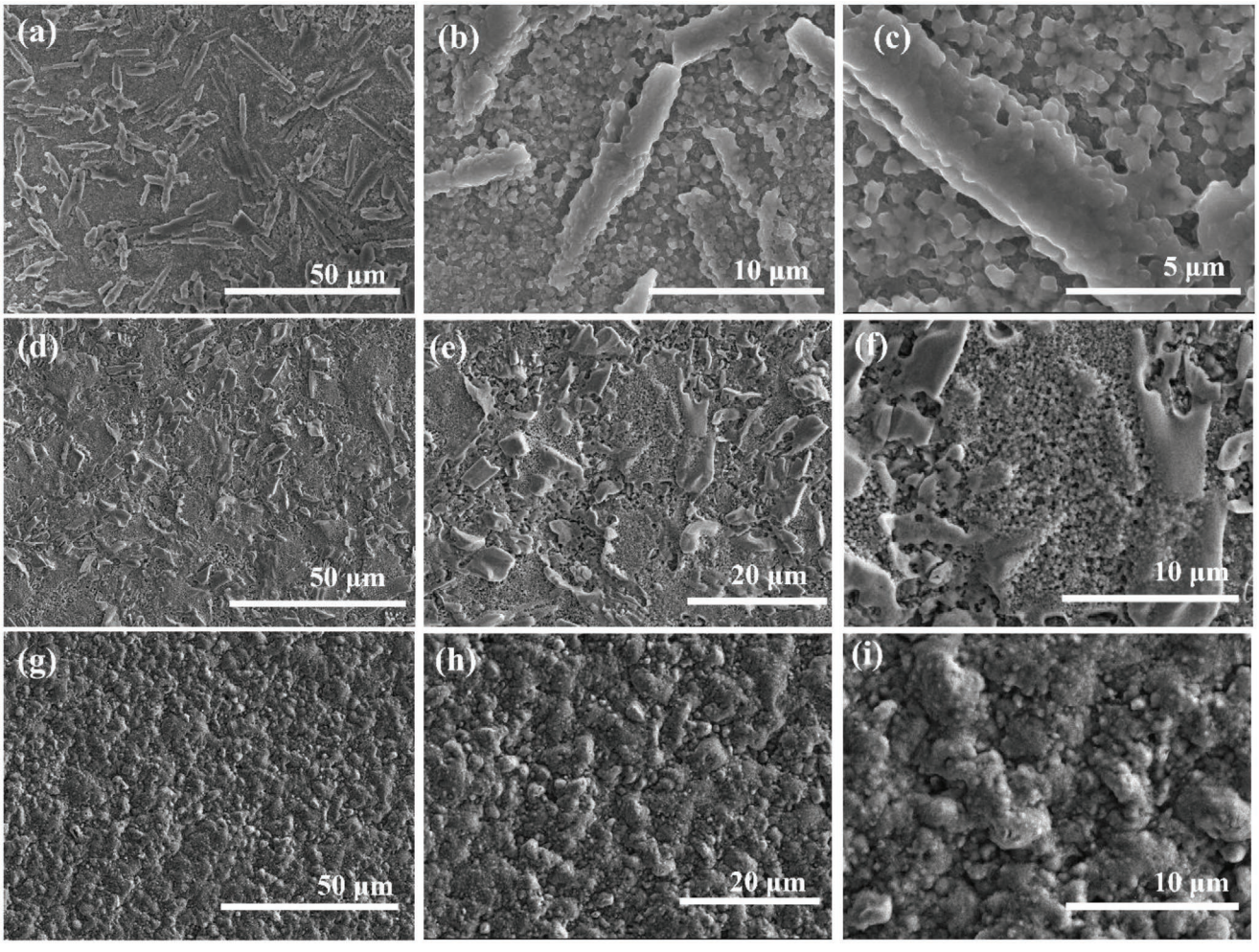

Figure 6. SEM images of S-MoS_2@PPCF-SSE cathode a–c) before cycling, d–f) fully charged to 3 V (vs Li/Li^+), and g–i) fully discharge to 1 V (vs Li/Li^+).

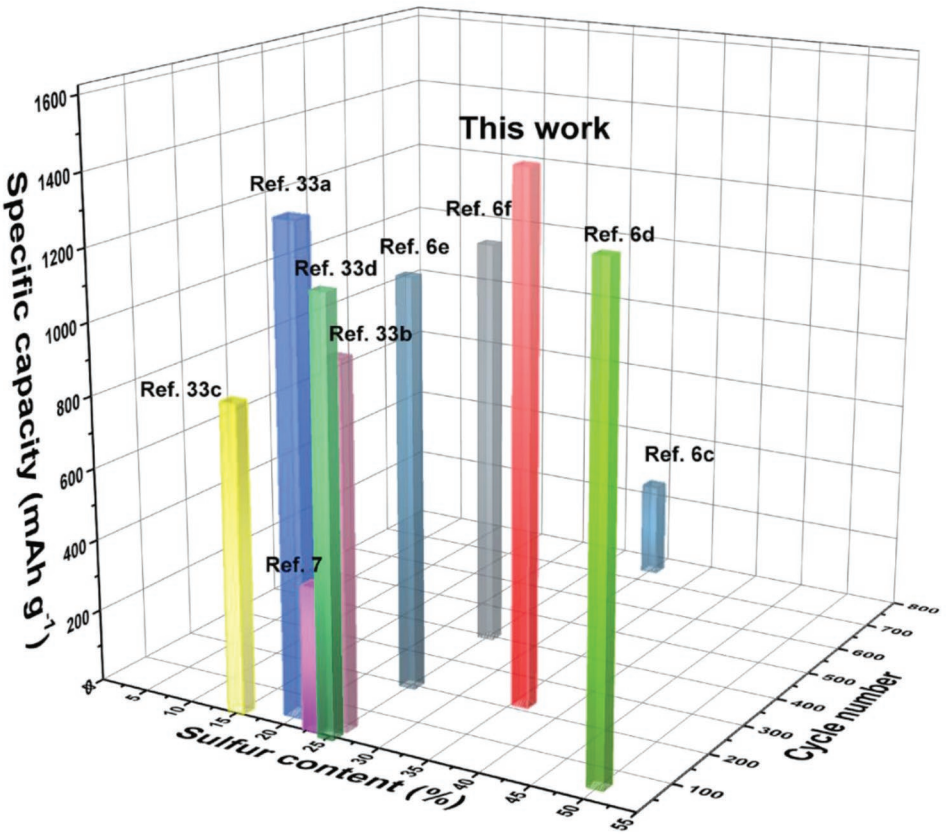

Figure 7. Comparison of specific capacity, sulfur content, and cycle number in different ASSLSBs.

conversion of sulfur to Li_2S, as shown in Figure 6g–i. Therefore, the electrode looks denser compared with the pristine one. Although the volume change exists in the cathode during the lithiation and delithiation, there are no cracks generated and no structural corruption demonstrating the excellent structural stability. Figure S7 (Supporting Information) shows the SEM images of the S-MoS_2@PPCF-SSE electrode after the rate test. The dense electrode maintains good integrity evidencing the excellent stability.

The Nyquist plots of S-MoS_2@PPCF-SSE full cell that was tested before and after cycling are compared in Figure S8 (Supporting Information). No huge difference is observed which can further prove the excellent stability. In contrast, there is an obvious impedance increase of 45 Ω in S-PPCF-SSE full cell after cycling due to the decomposition of SSE, as shown in Figure S9 (Supporting Information).

S-MoS_2@PPCF-SSE delivered an outstanding performance in ASSLSBs. **Figure 7** compares the sulfur content, cycling life, and capacity of S-MoS_2@PPCF-SSE with other reported ASSLSBs.[7,33] Detailed information is provided in Table S1 (Supporting Information). Obviously, our cell delivered the highest specific capacity of 1456 mAh g^{-1}, high sulfur loading of 36%, and the long cycling life of 220 cycles. The outstanding performance was mainly attributed to the utilization of the surface modified carbon additives, MoS_2@PPCF. First, the PPCF owns a high conductivity and high surface area which provides rich reaction sites for sulfur, therefore, resulting in the high mass loading of sulfur. Second, the highly ionic and electronic conductive MoS_2 layer benefits the charge transfer and boosts the conversion reaction kinetics of the sulfur, accompanied by enhanced sulfur utilization and high specific capacity. From the TGA result, the obtained MoS_2 weight fraction is ≈17.33%. With this amount of dosage, if the MoS_2 is electrically and ionically insulating, the electrochemical performance will be extremely low due to the isolation of electrons and ions. The much-improved electrochemical performance after MoS_2 coating in this work proved that MoS_2 has considerable electrical and ionic conductivity after lithiation. Third, the surface MoS_2 exhibits excellent chemical and electrochemical compatibility with sulfur and sulfide SSE as all of them belong to sulfide-based materials. The surface MoS_2 nanosheets reduced the contact area between PPCF and SSE which relieves the decomposition of sulfide SSE and contributes to a stable cycling behavior. All these merits contribute to the outstanding performance of this work presented in Figure 7.

3. Conclusion

In summary, we rationally designed an advanced carbon fiber decorated with vertically grown 1T/2H MoS_2 nanosheets to address the faced challenges in ASSLSBs, including the interface instability in sulfide SSE, the poor electronic and ionic conductivity, and the sluggish reaction kinetics. MoS_2, as metal

sulfide, owns excellent chemical and electrochemical stability with both sulfur and sulfide SSEs. Therefore, the MoS_2 nanosheets grown on carbon fiber effectively prevent the severe decomposition of sulfide SSE under high voltage beyond SSE electrochemical stability window. The presence of electrically conductive 1T phase MoS_2 and its uniform distribution on carbon fiber without aggregation improve electron transfer efficiency. The unique layered structure of MoS_2 can be intercalated by a large amount of Li ions and therefore facilitate ionic conductivity. As a result, the cell which owns high ion and electron transport network delivered a high initial discharge capacity of 1456 mAh g^{-1}, ultrahigh coulombic efficiency of ≈100%, high cycling stability with capacity retention of 78% over 220 cycles at 0.1 C, and outstanding rate performance of discharge capacity 1096 mAh g^{-1} at 1 C. The stable interface without side reactions and eliminated shuttle effects contribute to the extremely high initial coulombic efficiency. In contrast, the carbon fibers without MoS_2 obtained the lower initial discharge of 1185 mAh g^{-1} and the much poorer rate capacity of 220 mAh g^{-1} at 1 C due to more inferior interface stability and limited ionic conductivity at interface from degradation products. This study revealed the significance of the interface stabilization and functionalization of carbon additives for high-performance all-solid-state lithium-sulfur batteries.

4. Experimental Section

$Li_{5.4}PS_{4.4}Cl_{1.6}$ Preparation: The preparation of $Li_{5.4}PS_{4.4}Cl_{1.6}$ included a ball milling process and a subsequent annealing treatment. Briefly, Li_2S (Sigma-Aldrich, 99.98%), P_2S_5 (Sigma-Aldrich, 99%), and LiCl (Sigma-Aldrich, 99%) were mixed through ball milling for 10 h at 500 rpm in a vacuum atmosphere. Then the mixture electrolyte precursor was sealed in a glass tube and annealed at 510 °C for 2 h in the tube furnace.

Preparation of PPCF—Electrospinning: The synthesis of PPCF was based on a previous work.[16] Generally, PAN powder (Sigma-Aldrich, USA) possessing a molecular weight of 150 000 (Mw) was dissolved in N, N-dimethylformamide (DMF) (Fisher Scientific, 99.9%) to obtain the 15 wt% solution. The mixture was stirred for 24 h at room temperature to become a homogeneous solution. High voltage of 15 kV was applied.

Thermotreatment of PAN Precursor Nanofibers and Activation: The electrospun PAN precursor nanofibers were stabilized, carbonized, and activated to obtain the high-quality PPCF. The stabilization of as-electrospun nanofibers was carried out in a muffle furnace (GSL 1200X, MTI Corporation, Richmond, CA). The heating was in the air from room temperature to 250 °C with a heating rate of 1 °C min^{-1} and held at 250 °C for 1 h. The carbonization was conducted in a tubular furnace (GSL 1600X, MTI Corporation, Richmond, CA) in nitrogen (N_2) atmosphere. Then the stabilized PAN nanofibers were carbonized from room temperature to 1000 °C with a heating rate of 5 °C min^{-1}. The samples were held at 1000 °C for 1 h in flowing N_2, followed by automatically cooling down to room temperature. To obtain the activated carbon nanofibers, solid potassium hydroxide (KOH) was used to fabricate a porous structure. Carbon nanofibers were manually mixed with KOH fine powders with a weight ratio of 1:3. Then the mixture powders were activated to 1000 °C for 1 h in flowing N_2. After cooling to room temperature, the samples were purified against deionized water by multiple washing steps until the pH value of the water was stable. The dialyzed activated carbon nanofibers were then lyophilized and the evaporated PPCF was kept in a dry oven for future use.

Preparation of Hybrid 1T/2H MoS_2@PPCF: Hybrid 1T/2H MoS_2@PPCF was prepared by a hydrothermal method. In a typical synthesis process, 60 mg PPCF was dispersed in 15 mL deionized water using sonicated bath for 2 h. MoO_3 (18 mg, Fisher Scientific, USA), thioacetamide (21 mg, Sigma-Aldrich, USA), and urea (150 mg, Sigma-Aldrich, USA) were added in the as-prepared PPCF dispersion and stirring continued for 1 h. Then the sample was transferred to a 25 mL Teflon-sealed autoclave. The autoclave was kept in a furnace for 16 h at 200 °C. After cooling to room temperature, the hybrid 1T/2H MoS_2@PPCF were taken out and washed with ethanol three times. Then the samples were dialyzed against deionized water multiple times. The dialyzed MoS_2@PPCF was then lyophilized and evaporated at 60 °C.

Electrochemical Characterization of ASSLBs—Fabrication of All-Solid-State Li Sulfur Battery: ASSLSBs were fabricated by cold pressing method in the glovebox. For the cathode preparation, PPCF with/without MoS_2, sulfur, and $Li_{5.4}PS_{4.4}Cl_{1.6}$ were manually mixed in the weight ratio of 10/40/50 in a stainless-steel jar by mechanically milling for 10 h at a rotating speed of 400 rpm. Then the mixture was sealed in a glass tube and annealed from room temperature to 155 °C at the heating rate of 1 °C min^{-1} in the tube furnace. Then the mixture was held at 155 °C for 12 h and cooled down to room temperature with the ramp of 1 °C min^{-1}. Then mix the preprepared mixture with 3 wt% CNT and ball milling at 400 rpm speed for 2 h.

Rate and Cycling Performance: The rate and cycling measurements were performed with a protocol that cell first discharged to 1.0 V (vs Li/Li^+) at constant current, and then charged to 3.0 V (vs Li/Li^+) at constant current. The current was based on the capacity and mass of cathode active material. The rate performance was conducted C/20, C/10, C/5, C/2, and 1 C for five cycles, respectively. For the long cycling performance, all cells were activated for the first three cycles at C/20, then kept cycling at C/10.

GITT Measurement: All the cells were first discharged with a constant current rate of C/20 applied for 1 h and rested for 4 h until the voltage reached 1.0 V (vs Li/Li^+). And then the cells were charged with same current rate applied for 1 h and rested for 4 h until the voltage reached 3.0 V (vs Li/Li^+).

Materials Characterization: XRD was conducted on PANalytical/Philips X'Pert Pro with Cu Kα radiation. Raman spectra were measured on a Thermo Scientific DXR with 532 nm laser excitation. The SEM and energy-dispersive X-ray spectroscopy (EDS) mapping were characterized by SEM (JEPL JSM 7000F). Sulfur loading in the composites cathode was determined from TGA measurement (TA Q50, Inc.) in N_2 atmosphere at a heating rate of 10 °C min^{-1}. TEM and EDS mapping images were tested on the Cs-corrected TEM/STEM-FEI Titan Themis 300. The chemical structure comparisons of the samples were analyzed by XPS (Thermo Scientific K-Alpha).

Supporting Information

Supporting Information is available from the Wiley Online Library or from the author.

Acknowledgements

H.Z. and X.S. acknowledge the financial support from National Science Foundation under Award No. CBET-ES-1924534. The authors acknowledge the Northeastern University for Renewable Energy Technology (NUCRET) for sharing the XRD facilities. The authors thank Dr. Joshua Gallaway in Chemical Engineering of Northeastern University for the sharing of Raman measurements. The authors also acknowledge the Center for Nanoscale Systems (CNS) Harvard for providing the access to their XPS facility.

Conflict of Interest

The authors declare no conflict of interest.

Data Availability Statement

Research data are not shared.

Keywords

all-solid-state lithium-sulfur batteries, carbon fibers, charge transfer, interface stabilization, molybdenum disulfide, sulfide solid-state electrolyte

Received: March 10, 2022
Revised: May 9, 2022
Published online:

[1] a) J. Lu, Z. Chen, Z. Ma, F. Pan, L. A. Curtiss, K. Amine, *Nat. Nanotechnol.* **2016**, *11*, 1031; b) X. Zeng, M. Li, D. Abd El-Hady, W. Alshitari, A. S. Al-Bogami, J. Lu, K. Amine, *Adv. Energy Mater.* **2019**, *9*, 1900161; c) G. Harper, R. Sommerville, E. Kendrick, L. Driscoll, P. Slater, R. Stolkin, A. Walton, P. Christensen, O. Heidrich, S. Lambert, *Nature* **2019**, *575*, 75.

[2] R. Fakhry, S. Yeh, https://www.nrdc.org/sites/default/files/2030-biden-climate-pollution-ib.pdf (accessed: March 2021).

[3] Z. P. Cano, D. Banham, S. Ye, A. Hintennach, J. Lu, M. Fowler, Z. Chen, *Nat. Energy* **2018**, *3*, 279.

[4] S. Evers, L. F. Nazar, *Acc. Chem. Res.* **2013**, *46*, 1135.

[5] X. Yang, X. Li, K. Adair, H. Zhang, X. Sun, *Electrochem. Energy Rev.* **2018**, *1*, 239.

[6] a) P. Zhu, C. Yan, J. Zhu, J. Zang, Y. Li, H. Jia, X. Dong, Z. Du, C. Zhang, N. Wu, *Energy Storage Mater.* **2019**, *17*, 220; b) M. Nagao, A. Hayashi, M. Tatsumisago, *Electrochim. Acta* **2011**, *56*, 6055; c) X. Yao, N. Huang, F. Han, Q. Zhang, H. Wan, J. P. Mwizerwa, C. Wang, X. Xu, *Adv. Energy Mater.* **2017**, *7*, 1602923; d) H. Nagata, Y. Chikusa, *J. Power Sources* **2014**, *263*, 141; e) L.-P. Hou, H. Yuan, C.-Z. Zhao, L. Xu, G.-L. Zhu, H.-X. Nan, X.-B. Cheng, Q.-B. Liu, C.-X. He, J.-Q. Huang, *Energy Storage Mater.* **2020**, *25*, 436; f) Y. Zhang, T. Liu, Q. Zhang, X. Zhang, S. Wang, X. Wang, L. Li, L.-Z. Fan, C.-W. Nan, Y. Shen, *J. Mater. Chem. A* **2018**, *6*, 23345; g) Q. Zhang, N. Huang, Z. Huang, L. Cai, J. Wu, X. Yao, *J. Energy Chem.* **2020**, *40*, 151.

[7] M. Agostini, Y. Aihara, T. Yamada, B. Scrosati, J. Hassoun, *Solid State Ionics* **2013**, *244*, 48.

[8] a) J. He, G. Hartmann, M. Lee, G. S. Hwang, Y. Chen, A. Manthiram, *Energy Environ. Sci.* **2019**, *12*, 344; b) Y. You, Y. Ye, M. Wei, W. Sun, Q. Tang, J. Zhang, X. Chen, H. Li, J. Xu, *Chem. Eng. J.* **2019**, *355*, 671.

[9] R. Chen, J. Shen, K. Chen, M. Tang, T. Zeng, *Appl. Surf. Sci.* **2021**, *566*, 150651.

[10] a) E. Cha, M. D. Patel, J. Park, J. Hwang, V. Prasad, K. Cho, W. Choi, *Nat. Nanotechnol.* **2018**, *13*, 337; b) J. Fu, P. Yu, N. Zhang, G. Ren, S. Zheng, W. Huang, X. Long, H. Li, X. Liu, *Energy Environ. Sci.* **2019**, *12*, 1404.

[11] L. Yu, Q. Su, B. Li, L. Huang, G. Du, S. Ding, W. Zhao, M. Zhang, B. Xu, *Chem. Eng. J.* **2022**, *429*, 132479.

[12] A. Kızılaslan, T. Çetinkaya, H. Akbulut, *Adv. Mater. Interfaces* **2020**, *7*, 2001020.

[13] a) X. Geng, W. Sun, W. Wu, B. Chen, A. Al-Hilo, M. Benamara, H. Zhu, F. Watanabe, J. Cui, T.-P. Chen, *Nat. Commun.* **2016**, *7*, 10672; b) G. Eda, H. Yamaguchi, D. Voiry, T. Fujita, M. Chen, M. Chhowalla, *Nano Lett.* **2011**, *11*, 5111.

[14] Y. Pan, L. Gong, X. Cheng, Y. Zhou, Y. Fu, J. Feng, H. Ahmed, H. Zhang, *ACS Nano* **2020**, *14*, 5917.

[15] C. Lu, W.-w. Liu, H. Li, B. K. Tay, *Chem. Commun.* **2014**, *50*, 3338.

[16] X. Sun, Q. Li, D. Cao, Y. Wang, A. Anderson, H. Zhu, *Small* **2021**, 2105678.

[17] Y. Li, K. Chang, Z. Sun, E. Shangguan, H. Tang, B. Li, J. Sun, Z. Chang, *ACS Appl. Energy Mater.* **2019**, *3*, 998.

[18] K. Chang, X. Hai, H. Pang, H. Zhang, L. Shi, G. Liu, H. Liu, G. Zhao, M. Li, J. Ye, *Adv. Mater.* **2016**, *28*, 10033.

[19] M. Chen, X. Yin, M. Reddy, S. Adams, *J. Mater. Chem. A* **2015**, *3*, 10698.

[20] X. Shan, S. Zhang, N. Zhang, Y. Chen, H. Gao, X. Zhang, *J. Colloid Interface Sci.* **2018**, *510*, 327.

[21] F. Xiong, Z. Cai, L. Qu, P. Zhang, Z. Yuan, O. K. Asare, W. Xu, C. Lin, L. Mai, *ACS Appl. Mater. Interfaces* **2015**, *7*, 12625.

[22] a) Y. Yu, G.-H. Nam, Q. He, X.-J. Wu, K. Zhang, Z. Yang, J. Chen, Q. Ma, M. Zhao, Z. Liu, *Nat. Chem.* **2018**, *10*, 638; b) S. S. Chou, N. Sai, P. Lu, E. N. Coker, S. Liu, K. Artyushkova, T. S. Luk, B. Kaehr, C. J. Brinker, *Nat. Commun.* **2015**, *6*, 8311.

[23] Q. Tang, D.-E. Jiang, *Chem. Mater.* **2015**, *27*, 3743.

[24] X. Geng, W. Sun, W. Wu, B. Chen, A. Al-Hilo, M. Benamara, H. Zhu, F. Watanabe, J. Cui, T.-P. Chen, *Nat. Commun.* **2016**, 7.

[25] S. Shi, Z. Sun, Y. H. Hu, *J. Mater. Chem. A* **2018**, *6*, 23932.

[26] Y. Jiao, A. M. Hafez, D. Cao, A. Mukhopadhyay, Y. Ma, H. Zhu, *Small* **2018**, *14*, 1800640.

[27] D. Cao, Y. Zhang, A. M. Nolan, X. Sun, C. Liu, J. Sheng, Y. Mo, Y. Wang, H. Zhu, *Nano Lett.* **2019**, *20*, 1483.

[28] Y. Zhang, Y. Sun, L. Peng, J. Yang, H. Jia, Z. Zhang, B. Shan, J. Xie, *Energy Storage Mater.* **2019**, *21*, 287.

[29] Y. Yang, X. Sun, Z. Cheng, A. Mukhopadhyay, A. Natan, C. Liu, D. Cao, H. Zhu, *ACS Appl. Energy Mater.* **2020**, *3*, 6249.

[30] J. Auvergniot, A. Cassel, J.-B. Ledeuil, V. Viallet, V. Seznec, R. Dedryvère, *Chem. Mater.* **2017**, *29*, 3883.

[31] J. Auvergniot, A. Cassel, D. Foix, V. Viallet, V. Seznec, R. Dedryvère, *Solid State Ionics* **2017**, *300*, 78.

[32] a) D. H. Tan, E. A. Wu, H. Nguyen, Z. Chen, M. A. Marple, J.-M. Doux, X. Wang, H. Yang, A. Banerjee, Y. S. Meng, *ACS Energy Lett.* **2019**, *4*, 2418; b) Y. Zhu, X. He, Y. Mo, *ACS Appl. Mater. Interfaces* **2015**, *7*, 23685.

[33] a) M. Chen, S. Adams, *J. Solid State Electrochem.* **2015**, *19*, 697; b) K. Suzuki, D. Kato, K. Hara, T.-a. Yano, M. Hirayama, M. Hara, R. Kanno, *Electrochim. Acta* **2017**, 258; c) U. Ulissi, S. Ito, S. M. Hosseini, A. Varzi, Y. Aihara, S. Passerini, *Adv. Energy Mater.* **2018**, *8*, 1801462; d) J. Nguyen, B. Fleutot, R. Janot, *Solid State Ionics* **2018**, *315*, 26.